# High-order-helix point spread functions for monocular three-dimensional imaging with superior aberration robustness

Berlich, Ren; Stallinga, Sjoerd

**DOI**
10.1364/OE.26.004873

**Publication date**
2018

**Document Version**
Final published version

**Published in**
Optics Express

**Citation (APA)**
Berlich, R., & Stallinga, S. (2018). High-order-helix point spread functions for monocular three-dimensional imaging with superior aberration robustness. *Optics Express*, *26*(4), 4873-4891. https://doi.org/10.1364/OE.26.004873

Research Article | Vol. 26, No. 4 | 19 Feb 2018 | OPTICS EXPRESS 4873

Optics EXPRESS

# High-order-helix point spread functions for monocular three-dimensional imaging with superior aberration robustness

RENÉ BERLICH[1,*] AND SJOERD STALLINGA[2]

[1]*Fraunhofer Institute for Applied Optics and Precision Engineering, Albert-Einstein Str. 7, 07745 Jena, Germany*

[2]*Department of Imaging Physics, Delft University of Technology, Lorentzweg 1, 2628 CJ Delft, The Netherlands*

*∗rene.berlich@iof.fraunhofer.de*

**Abstract:** An approach for designing purely refractive optical elements that generate engineered, multi-order-helix point spread functions (PSFs) with large peak separation for passive, optical depth measurement is presented. The influence of aberrations on the PSF's rotation angle, which limits the depth retrieval accuracy, is studied numerically and analytically. It appears that only Zernike modes with an azimuthal index that is an integer multiple of the number of PSF peaks introduce PSF rotation, and hence a depth estimation errors. This implies that high-order-helix designs have superior robustness with respect to aberrations. This is experimentally demonstrated by imaging an extended scene in the presence of severe system aberrations using novel, cost-efficient phase elements based on UV-replication on the wafer-scale.



**OCIS codes:** (110.1758) Computational imaging; (110.6880) Three-dimensional image acquisition; (110.7348) Wavefront encoding.

## References and links

1. E. R. Dowski and W. T. Cathey, "Extended depth of field through wave-front coding," Appl. Opt. **34**, 1859–1866 (1995).
2. A. Castro and J. Ojeda-Castañeda, "Asymmetric phase masks for extended depth of field," Appl. Opt. **43**, 3474 (2004).
3. Q. Yang, L. Liu, and J. Sun, "Optimized phase pupil masks for extended depth of field," Opt. Commun. **272**, 56–66 (2007).
4. A. Greengard, Y. Y. Schechner, and R. Piestun, "Depth from diffracted rotation," Opt. Lett. **31**, 181–3 (2006).
5. S. R. P. Pavani and R. Piestun, "High-efficiency rotating point spread functions," Opt. Express **16**, 3484–3489 (2008).
6. S. Prasad, "Rotating point spread function via pupil-phase engineering," Opt. Lett. **38**, 585–587 (2013).
7. S. R. P. Pavani and R. Piestun, "Three dimensional tracking of fluorescent microparticles using a photon-limited double-helix response system," Opt. Express **16**, 22048–22057 (2008).
8. S. R. P. Pavani, A. Greengard, and R. Piestun, "Three-dimensional localization with nanometer accuracy using a detector-limited double-helix point spread function system," Appl. Phys. Lett. **95**, 021103 (2009).
9. G. Grover, S. Quirin, C. Fiedler, and R. Piestun, "Photon efficient double-helix PSF microscopy with application to 3D photo-activation localization imaging," Biomed. Opt. Express **2**, 3010–3020 (2011).
10. A. Barsic, G. Grover, and R. Piestun, "Three-dimensional super-resolution and localization of dense clusters of single molecules," Sci. Reports **4**, 5388 (2014).
11. C. Roider, A. Jesacher, S. Bernet, and M. Ritsch-Marte, "Axial super-localisation using rotating point spread functions shaped by polarisation-dependent phase modulation," Opt. Express **22**, 4029–4037 (2014).
12. S. Quirin, S. R. P. Pavani, and R. Piestun, "Optimal 3D single-molecule localization for superresolution microscopy with aberrations and engineered point spread functions," Proc. Natl. Acad. Sci. **109**, 675–679 (2012).
13. C. Roider, R. Heintzmann, R. Piestun, and A. Jesacher, "Deconvolution approach for 3D scanning microscopy with helical phase engineering," Opt. Express **24**, 15456 (2016).
14. S. Quirin and R. Piestun, "Depth estimation and image recovery using broadband, incoherent illumination with engineered point spread functions [Invited]," Appl. Opt. **52**, A367–A376 (2013).
15. R. Berlich, A. Bräuer, and S. Stallinga, "Single shot three-dimensional imaging using an engineered point spread function," Opt. Express **24**, 5946 (2016).
16. S. Ghosh and C. Preza, "Characterization of a three-dimensional double-helix point-spread function for fluorescence microscopy in the presence of spherical aberration," J. Biomed. Opt. **18**, 036010 (2013).

#318101 https://doi.org/10.1364/OE.26.004873
Journal © 2018 Received 20 Dec 2017; revised 5 Feb 2018; accepted 5 Feb 2018; published 15 Feb 2018

17. Z. Cao and K. Wang, "Effects of astigmatism and coma on rotating point spread function," Appl. Opt. **53**, 7325–7330 (2014).
18. M. Baránek, P. Bouchal, M. Šiler, and Z. Bouchal, "Aberration resistant axial localization using a self-imaging of vortices," Opt. Express **23**, 15316 (2015).
19. R. Piestun and J. Shamir, "Generalized propagation-invariant wave fields," J. Opt. Soc. Am. A **15**, 3039–3044 (1998).
20. R. Piestun, Y. Schechner, and J. Shamir, "Propagation-invariant wave fields with finite energy," JOSA A **17**, 294–303 (2000).
21. G. Grover and R. Piestun, "New approach to double-helix point spread function design for 3D super-resolution microscopy," Proc. SPIE **8590**, 85900M (2013).
22. K. Itoh, "Analysis of the Phase Unwrapping Algorithm," Appl. Opt. **21**, 2470 (1982).
23. D. Baddeley, M. B. Cannell, and C. Soeller, "Three-dimensional sub-100 nm super-resolution imaging of biological samples using a phase ramp in the objective pupil," Nano Res. **4**, 589–598 (2011).
24. A. N. Simonov and M. C. Rombach, "Passive ranging and three-dimensional imaging through chiral phase coding," Opt. Lett. **36**, 115–117 (2011).
25. M. Born and E. Wolf, *Principles of Optics: Electromagnetic Theory of Propagation, Interference and Diffraction of Light* (Elsevier, 2013).
26. V. N. Mahajan, "Line of sight of an aberrated optical system," J. Opt. Soc. Am. A **2** (1985).
27. H.-C. Eckstein, U. D. Zeitner, R. Leitel, M. Stumpf, P. Schleicher, A. Bräuer, and A. Tünnermann, "High dynamic grayscale lithography with an LED-based micro-image stepper," Proc. SPIE **9780**, 97800T (2016).
28. K.-H. Haas and H. Wolter, "Synthesis, properties and applications of inorganic–organic copolymers (ORMOCERs)," Curr. Opin. Solid State Mater. Sci. **4**, 571–580 (1999).

## 1. Introduction

The depth dependence of the Point Spread Function (PSF) of an imaging system can be customized by engineering the pupil phase with a Computer Generated Hologram (CGH). This approach has been widely studied with the goal to extend the depth of focus of conventional imaging systems [1–3]. In addition, it has gained interest for monocular, three-dimensional imaging [4]. Phase element designs have been proposed that generate two separated PSF peaks with a defocus dependent, double-helix shaped rotation [5, 6]. If the relationship between the rotation angle $\alpha$ and the distance of an object point $z$ is known, a measurement of $\alpha$ enables retrieving the axial location of an object point in addition to its lateral location. So far, this method has mainly been applied for three-dimensional particle localization and tracking [7–13]. Further studies have demonstrated that the entire depth map of an extended, three-dimensional scene can be obtained for a broadband illumination [14, 15].

Previous studies have commonly considered idealized optical systems with an imaging performance close to the diffraction limit. The imaging performance of state-of-the-art optical systems in application fields such as machine vision, automotive or consumer electronics is, however, commonly far away from the diffraction limit. It is therefore essential to investigate how susceptible helical PSFs are to aberrations and how the rotation of the engineered PSF and ultimately the depth retrieval may be corrupted. In fact, the required calibration of the relationship between the rotation angle $\alpha$ and the object distance $z$ only partially accounts for aberration introduced rotation. The calibration step is commonly performed close to the optical axis, which does not allow for compensating for the effect of off-axis system aberrations such as astigmatism. A calibration of the entire field of view of the pupil engineered system would be necessary in order to eliminate respective rotation angle uncertainties. Moreover, this characterization would have to be performed for each nominal object distance setting, which requires an immense calibration effort. In addition, aberration conditions may vary for different application scenarios, e.g. due to thermally induced effects or imaging through thick media. Thus, the question arises if the influence could be mitigated by altering the design of the rotating PSF.

The particular influence of primary spherical aberration, as well as coma and astigmatism has been investigated in the literature for the specific case of double-helix PSFs [16–18]. In this paper, we study the robustness for aberrations of helical PSFs in a generalized framework in which we consider designs with $N$ peaks ($N = 2, 3, 4, \ldots$). The aim of this analysis is to provide the necessary foundation for balancing the impact of different aberrations on the rotation of the

PSF in order to develop high accuracy, pupil engineered optical systems for 3D image acquisition. Furthermore, we demonstrate how high-order-helix designs that feature more than two PSF peaks provide improved robustness regarding the rotation of the PSF with defocus. The respective designs thus allow for less stringent requirements on the optical system, e.g. with respect to the residual wave front error, which reduces system complexity and costs. Especially astigmatism is of considerable importance, as it scales quadratically with the field coordinates, and therefore usually dominates over other aberrations that scale with higher powers of the field coordinates.

Initially, we present a new design method for higher order helical PSFs and evaluate its performance in section 2. In section 3, we analyze the sensitivity of the PSF rotation to different aberrations using numerical and theoretical means. Experimental results are presented in section 4 and the main results of the paper are concluded in section 5.

## 2. Multi-order-helix designs

### *2.1. Design approach*

A design approach to generate PSF distributions that provide a depth dependent rotation was initially introduced based on a set Bessel beams [19]. Subsequently, these designs were described using a composition of Gauss-Laguerre (GL) modes [20] and extended towards phase only elements [5, 21]. An alternative design method using a set of Fresnel zones to generate rotating, single-helix PSFs ($N = 1$) was described by Prasad in [6] and extended for double-helix shapes by Roider et al. in [11]. These two design approaches provide a basis for customized double-helix CGH designs that are, however, limited in different ways. On the one hand, we find that the GL mode based designs provide limited capability to generate largely separated PSF peaks with an extended rotation range. In particular, the iterative optimization results in undesired side lobes that limit the depth retrieval accuracy as well as the image quality. On the other hand, the Fresnel zone designs do not allow for direct optimization of the PSF peak confinement over a specific axial range of interest. Moreover, both methods lead to very complex CGH designs with a significant number of phase discontinuities and dislocations that degrade the PSF shape when imaging using a broad wavelength spectrum.

Here, we propose a novel phase element design routine to overcome these limitations and moreover to allow for generating generalized $N$th order helix PSFs. To this end, we initially generalize the Fresnel zone design approach [6, 11] by exploiting three main design parameters. The number of zones that lie within the phase element radius $R$ is defined by the design parameter $L$. Each of the $l = 1, ..., L$ zones is bounded by circles of radius $R_{l-1}$ and $R_l$, where $R_l = R(l/L)^\epsilon$. The second design parameter $\epsilon$ can be used to tailor the trade-off between the helix peak confinement and the shape invariance during rotation. The phase of the $l$th ring of the CGH is given by

$$\Phi_l(\phi) = [(l-1)\,N + 1]\,\phi \qquad (1)$$

where $\phi$ is the azimuthal coordinate. Here, we consider a third design parameter $N$ in the phase definition, which represents a generalization of existing designs [6, 11]. It directly defines the peak number of the generalized multi-order-helix PSF. Note that for $N = 1$, Eq. (1) reduces to the original single-helix phase element design proposed in [6]. In general, the peak separation, the rotation rate as well as the total depth range of the corresponding, engineered PSF are jointly influenced by the three design parameters $[N, L, \epsilon]$. On the one hand, the maximum depth range is limited by ambiguities in case of a rotation beyond $[-\pi/N, \pi/N]$ since the depth retrieval is based on relating the rotation angle $\alpha$ to the object distance $z$. Consequently, a high number of peaks also reduces the available depth range. On the other hand, the PSF rotates at a rate $1/(N \cdot L)$ rad per unit defocus change for the particular case of $\epsilon = 0.5$, according to the analytical PSF approximation given in [6]. Hence, the respective maximum, unambiguous defocus range equals $2\pi L$, which is independent of the peak number $N$. This range can be related to the maximum

Optics EXPRESS

available depth range $\Delta z_{\max}$ of the pupil engineered optical system according to

$$\Delta z_{\max} = \frac{2\lambda d_0^2 L}{R^2 + 2\lambda l d_0 L} \quad , \tag{2}$$

where the variables $\lambda$, $d_0$ and $R$ denote the wavelength, the object distance from the entrance pupil and the entrance pupil radius, respectively. The relationship is more complex for a general parameter $\epsilon$, but it appears empirically that the depth range increases for decreasing $\epsilon$.

The generalized Fresnel zone elements are considered as start designs for the following design process. In fact, the parameter set $[N, L, \epsilon]$ directly determines the number of peaks, the peak separation, the rotation rate, as well as the maximum depth range of the final element. The individual steps of the overall design process are depicted in Fig.1 for the design of a phase distribution $\Phi_p$ of exemplary double- and triple-helix CGHs. For illustration purposes, Fig.1 additionaly provides the corresponding in-focus PSF distributions, which are calculated based on a Fourier transformation and considering a circular aperture. Figure 1(a) and 1(b) show the two Fresnel zone start design examples with design parameters $[N, L, \epsilon]$ equal to $[2, 16, 0.8]$ and $[3, 11, 0.8]$, respectively. Note that the corresponding PSFs provide comparable peak distances with respect to the optical axis. We find that each of the $N$ PSF peaks can be allocated to a dedicated circular sector of the Fresnel zone design with azimuthal extensions of $2\pi/N$, respectively. Accordingly, the next design step only considers a single sector of the overall pupil area. In fact, restricting the design optimization to an individual subsection is essential in order to circumvent phase dislocations in the final phase element design. Figure 1(c) and 1(d) illustrate the respective sections and the corresponding PSF peak. Next, a modified version of the iterative optimization approach as proposed for the GL mode design approach [5] is applied. It is based on an Iterative Fourier Transform Algorithm (IFTA) and applies two main constraints. The first constraint maximizes the energy in the main lobes of the helical PSF for a high peak confinement. The second constraint enforces a phase only transfer function in the aperture plane. In contrast to the original method, the third constraint in the GL modal plane is voided and the pupil aperture is restricted to the circular sector of a single peak. The optimization results in a well-confined peak over a rotation range of $2\pi/N$ even for the large peak separations of the two examples, which are on the order of ten times the peak diameter. The obtained exemplary phase distributions are shown in Fig. 1(e) and 1(f). The remaining $N-1$ circular sections of the CGH are subsequently filled with rotated copies of the optimized subarea as illustrated in Fig. 1(g) and 1(h). This leads to $N$ equal peaks in the focal plane, which form a completely symmetric multi-order-helix PSF. Note that phase dislocations inside the CGH are only located at distinct lines, which separate the individual circular section. The phase distributions within each section can thus be easily transformed into continuous profiles by using a conventional one-dimensional phase unwrapping method [22]. Figure 1(i) and 1(j) show the respective profiles for the two design examples. We emphasize that these continuous pupil phase shifts can be realized by purely refractive (free-form) optical elements. These elements provide an improved performance when a broad spectral range is used for imaging. They offer minimized color artifacts, which is particularly critical for designs with a large peak separation. In fact, the double-helix element shown in Fig. 1(i) is similar to the double wedge type designs that have already been proposed in the literature [23, 24]. However, our design approach enables an improved PSF confinement with minimized peak spreading over a customized defocus range as shown in the next subsection.

### 2.2. Performance evaluation

The appropriateness of engineered PSFs for depth estimation is typically measured by the Cramér-Rao Lower Bound (CRLB) [5, 8, 14], which quantifies the theoretical limit of precision

Optics EXPRESS

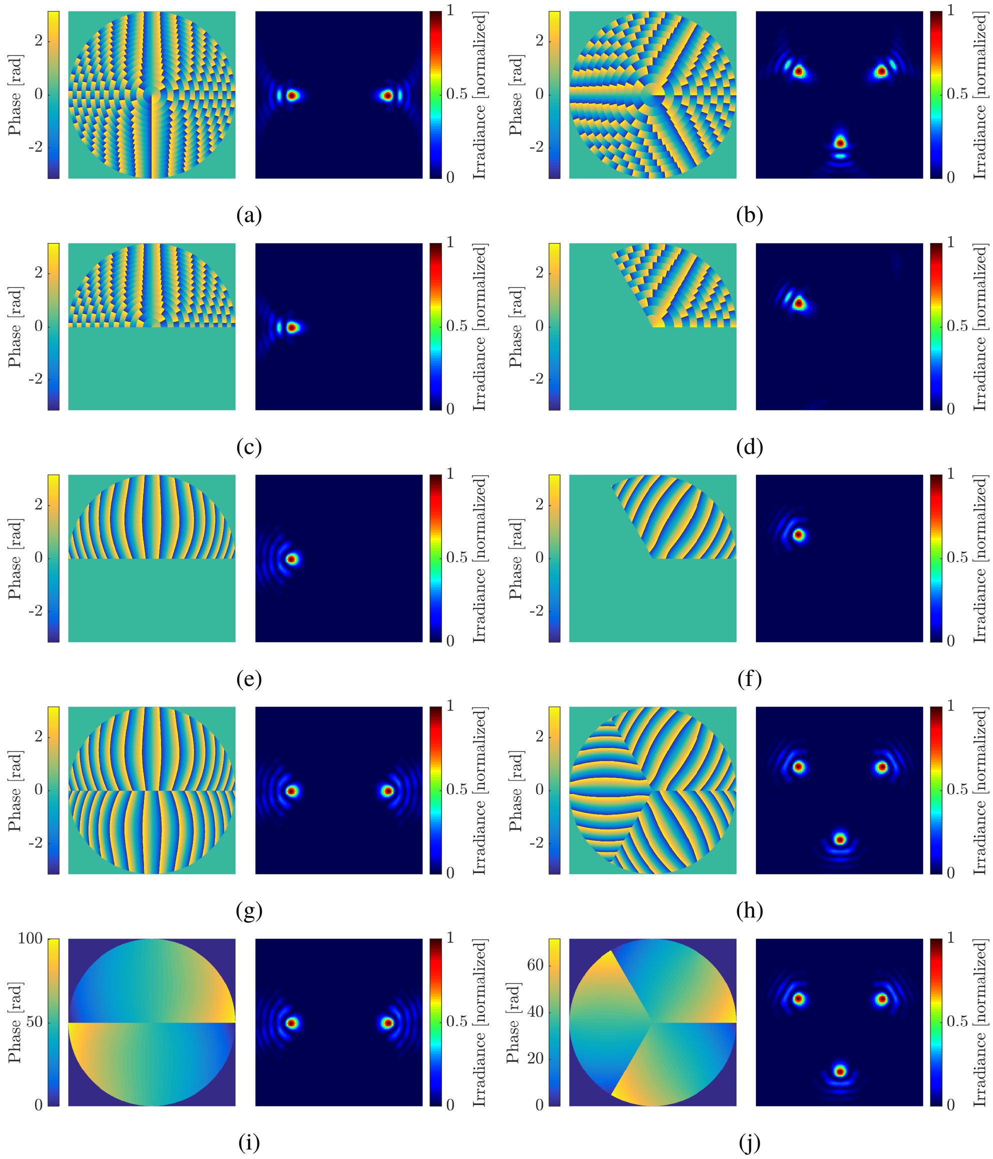


Fig. 1. The individual steps of the proposed design process for multi-order-helix PSFs are exemplary illustrated for a double- (left column) and a triple- (right column) helix design. The phase distributions $\Phi_p$ as well as the corresponding PSFs are shown for the individual design steps. The Fresnel zone start designs (a,b) are initially truncated to an angular section, dedicated to a single PSF peak (c,d). The respective section is optimized for a high peak confinement (e,f) and subsequently used to fill the overall phase element with rotated copies (g,h). A purely refractive design is finally obtained by phase unwrapping in an optional step (i,j).

Optics EXPRESS

in axial ranging. The CRLB for an imaged, broadband point source is given by [14]

$$\sigma_{\text{CRLB}}^{-2}(z) = \frac{1}{\sigma_N^2} \sum_{v=1}^{V} \sum_{w=1}^{W} \left( \frac{\partial}{\partial z} H'[v, w; z] \right)^2 \tag{3}$$

where

$$H'[v, w; z] = \int_{\lambda_1}^{\lambda_2} \eta(\lambda) H[v, w; z; \lambda] \, d\lambda \tag{4}$$

is the incoherent superposition of the discretely sampled spectral PSF components and $\sigma_{\text{CRLB}}$ defines the standard deviation of the lower limit to measurement precision. A system operating in the detector-limited regime is assumed in Eq. (3), which is applicable for imaging extended scenes with a generally high background level using low-end cameras with high readout noise. Accordingly, the readout noise and the shot noise of the background irradiance level dominate the shot noise from the peak signal. The parameter $\sigma_N^2$ denotes the variance of per-pixel noise, which is taken to be the sum of the two dominating noise contributions. Note that the three-dimensional PSF distribution $H'[v, w; z]$ is normalized such that their maximum irradiance is equal to one. A simplified, constant relative illumination spectrum $\eta(\lambda) = 1$, which ranges from $\lambda_1 = 450$ to $\lambda_2 = 650$ *nm*, is considered in the following.

The goal of the subsequent analysis is to compare the performance of different helical PSF designs under broadband imaging conditions. The optical system parameters used for the experimental study in section 4 are exemplarily applied for this investigation. A signal-to-noise ratio of 20 is assumed, which results in $\sigma_N = 0.05$. The designs under investigation include the double-helix Fresnel zone design, the optimized double- and triple-helix designs as well as the purely refractive double-helix design shown in Fig. 1(a), 1(g), 1(h) and 1(i), respectively. In addition, a nominal, clear aperture system is analysed as a reference. The broadband, axial distributions $H'[v, w; z]$ of the considered pupil functions are calculated at different object distances $z$ and illustrated in the top part of Fig. 2. The selected axial range of 600 *mm* corresponds to a rotation of approximately 180° of the double-helix PSF designs. The rotation continues beyond this range but the double-helix peaks start experiencing significant spreading. In fact, the triple-helix design is only optimized for a range of approximately 300 *mm* but continues rotating beyond this range with accelerated peak spreading as can be seen in Fig. 2.

The simulated axial PSF distributions in the top part of Fig. 2 qualitatively illustrate the improved peak confinement of the novel, double-helix CGH design over the entire rotation range in comparison to the double-helix Fresnel zone design. The CRLB analysis moreover allows for a quantitative comparison, which shows that $\sigma_{\text{CRLB}}$ is improved by a factor of 2 at the edges of the axial range of interest. In general, the proposed pupil engineered PSF designs feature superior values for $\sigma_{\text{CRLB}}$ that are at least an order of magnitude decreased compared to the clear aperture system, which is consistent with previous results reported in [4, 8, 14]. In addition, the PSF comparison of the refractive double-helix design with the diffractive elements demonstrates their improved peak confinement under broadband imaging conditions. In particular, the PSFs of the diffractive elements in Fig. 2 comprise increased peak spreading in addition to the presence of a central peak at the nominal object distance. Both impairments of the PSF shape originate from a mismatch of the $2\pi$ phase jumps in the CGH design at wavelength that differ from the nominal wavelength. Finally, Fig. 2 reveals that the novel triple-helix design comprises a reduced axial resolution limit around the nominal object distance in comparison to the optimized double-helix design. In contrast, the axial resolution limit is increased for defocus values of $|\Delta z| \gtrsim 100$ *mm*, which is in accordance with the reduced axial range that is considered for the design optimization.

Research Article | Vol. 26, No. 4 | 19 Feb 2018 | OPTICS EXPRESS 4879
Optics EXPRESS

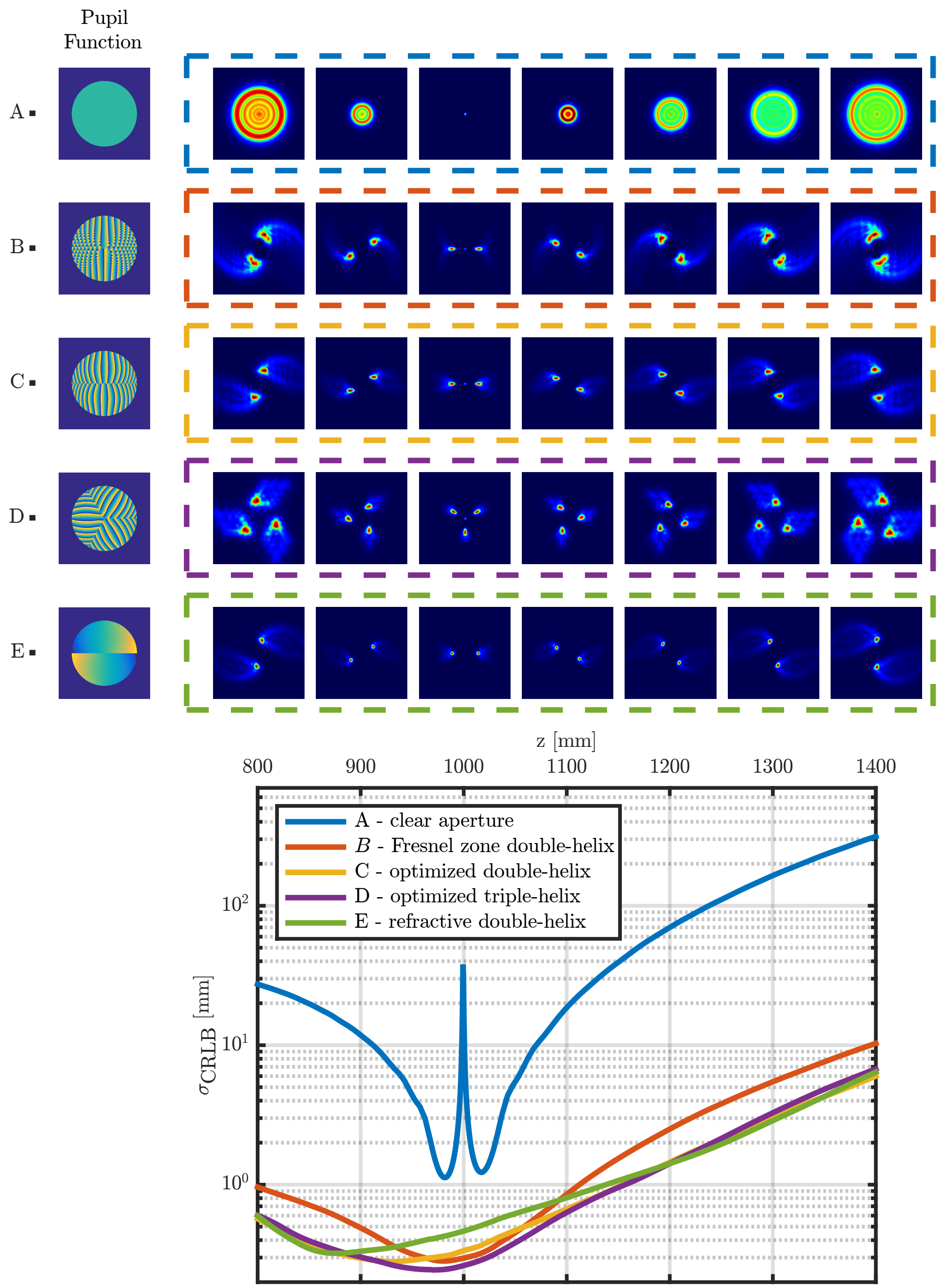


Fig. 2. Top: Simulated, axial PSF dependency $H'[v, w; z]$ of five considered pupil functions as indicated in the left part: A, nominal PSF for a clear aperture; B, Fresnel zone double-helix PSF; C, optimized double-helix PSF; D, optimized triple-helix PSF; E, refractive double-helix PSF. A broadband illumination spectrum ranging from 450 – 650 $nm$ and a nominal object distance of $z = 1000$ $mm$ are assumed. Note that the individual PSF plots are normalized to their respective maximum irradiance level for illustration purposes. Bottom: Corresponding axial dependencies of the standard deviation of the lower limit to measurement precision $\sigma_{\mathrm{CRLB}}$.

Optics EXPRESS

## 3. Influence of aberrations on PSF rotation

In the following investigation, the effect of individual optical aberrations on the rotation angle of multi-order-helix PSFs is analyzed. Initially, the influence is investigated by numerical simulations for the two design examples given in section 2 as well as a tetra-helix example with design parameters $[N, L, \epsilon] = [4, 8, 0.8]$. Note that no single peak design ($N = 1$) is considered, since it cannot be applied for 3D measurement using the approaches presented in [14, 15]. Finally, an analytic rotation assessment is provided for general, multi-helix CGH designs in order to obtain a theoretical understanding on which aberrations cause rotation. To this end, a general, quantitative measure for rotation of multi-order-helix PSFs is defined and evaluated in order to derive a general condition for identifying aberrations that result in a (false) PSF rotation.

### *3.1. Numerical investigation of PSF rotation*

The pupil phase $\Phi(u, v)$ of an aberrated, pupil engineered optical system is given by a superposition of the phase element part $\Phi_p$ and the aberrated part according to

$$\Phi(u, v) = \Phi_p(u, v) + \sum_{n,m} A_n^m \cdot Z_n^m(u, v)\,, \tag{5}$$

where $(u, v)$ denote the Cartesian coordinates of the pupil plane. The aberrated part is described by a set of Zernike polynomials $Z_n^m$ and their respective amplitudes $A_n^m$. The individual polynomials $Z_n^m$ are defined in polar coordinates by

$$Z_n^m(\rho, \phi) = R_n^m(\rho) \cos m\phi \tag{6}$$

for even and

$$Z_n^{-m}(\rho, \phi) = R_n^m(\rho) \sin m\phi \tag{7}$$

for odd polynomials, respectively. The term $R_n^m(\rho)$ denotes the radial dependency according to [25] and $(m, n)$ are non-negative integers that satisfy $m \le n$, $n - m =$ even. The effect of first order Zernike aberrations on the double- and triple-helix PSF distributions is qualitatively shown in Fig. 3. The amplitude $A_n^m$ of each Zernike aberration is successively increased in Fig. 3, which introduces an rms phase error in a range of $[0, \pi/2]$ rad. Note that the first three modes associated with piston, tip and tilt errors are omitted, since they do not affect the PSF shape. The actual depth retrieval using helical PSFs is based on the desired rotation with an increasing amplitude of defocus ($Z_2^0$). However, Fig. 3 reveals that other Zernike aberrations lead to distortions of the original PSF shape that also give rise to an apparent rotation. In order to quantify the effect on the rotation of the multi-order-helix PSF distributions, an overall rotation angle $\alpha$ is defined as the average

$$\alpha = \frac{1}{N} \sum_{j=1}^{N} \Delta\alpha_j\,, \tag{8}$$

where $\Delta\alpha_j$ is the difference between the individual peak angle with and without aberrations, respectively. Note that the individual angles $\Delta\alpha_j$ can be positive or negative depending on the rotation direction. The change of the overall rotation angle $\alpha$ with increasing amplitudes of the first 21 Zernike aberrations is shown in Fig. 4 for the three multi-order-helix designs under investigation. The individual values are obtained by fitting $N$ Gaussian peaks to the respective PSF distributions and extracting the fitted peak angle difference $\Delta\alpha_j$. The numerical fitting accuracy is on the order of $1°$ due to shape distortions and side lobes of the aberrated peaks. The overview in Fig. 4 demonstrates that the effect on the PSF rotation angle significantly depends on the particular Zernike mode as well as the order $N$ of the engineered PSF. Aberrations that cause a significant rotation, i.e. $|\alpha(\pi/2)| > 1°$, are highlighted by rectangular boxes in Fig. 4. An increasing defocus

Optics EXPRESS

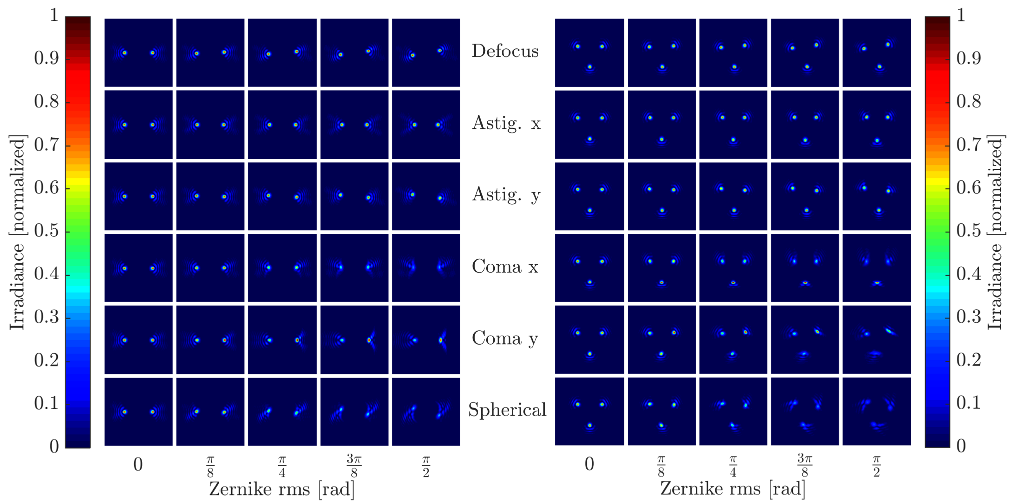


(a) Double-helix (b) Triple-helix

Fig. 3. Influence of primary Zernike aberrations on the shape of an engineered (a) double- and (b) triple-helix PSF design including the effect of defocus ($Z_2^0$) as well as first order astigmatism ($Z_2^{-2}$,$Z_2^2$), coma ($Z_3^{-1}$,$Z_3^1$) and spherical aberration ($Z_4^0$).

rms error leads to the desired linear change of $\alpha$ for all three design examples, as expected. It can be seen that primary spherical aberration ($Z_4^0$) results in a significant increase of the rotation angle $\alpha$ as well. In contrast, the numerical simulations reveal that coma ($Z_3^{-1}$, $Z_3^1$) does not lead to a change of the overall rotation angle $\alpha$. The effect of astigmatism ($Z_2^{-2}$, $Z_2^2$) depends on the particular CGH design. No rotation can be observed for the triple- and tetra-helix design, whereas the double-helix design is subject to significant rotation for astigmatism in $x$. In fact, the PSF distributions shown in Fig. 3(b) indicate that the individual peak angles of the triple-helix PSF vary indeed. However, the differences $\Delta\alpha_i$ appear to compensate each other. The results are in agreement with previous analyses of double-helix designs [16–18], which demonstrated a high rotation susceptibility to spherical aberration and astigmatism, but a robustness with respect to coma. A general trend can be observed in Fig. 4 that suggests that a higher number of peaks $N$ leads to less modes that cause significant PSF rotation. The simulations particularly suggest that the overall rotation angle is zero unless the mode order $m$ is a multiple of the PSF peak number $N$. In the following, we will develop a theoretical framework that explains this result.

### 3.2. Theoretical rotation assessment

Considering geometrical optics, the two-dimensional position vector $\vec{c}$ where a single ray intersects the image plane is determined by the local slope of the wave front $W(u, v)$ in the corresponding pupil location. The (coherent) superposition of all individual rays that emerge from an object point and pass through the pupil provides the centroid location of the PSF. As shown in [26], the centroid vector $\langle\vec{c}\rangle = (\langle c_x\rangle, \langle c_y\rangle)$ of the PSF according to wave optics is identical with that according to geometrical optics. It can be obtained by integrating the gradient distribution of the wavefront $W(u, v)$ over the exit pupil (EP) area according to:

$$\langle\vec{c}\rangle = -\frac{D}{E}\iint_{\mathrm{EP}} \vec{\nabla}W(u, v)\, du dv \tag{9}$$

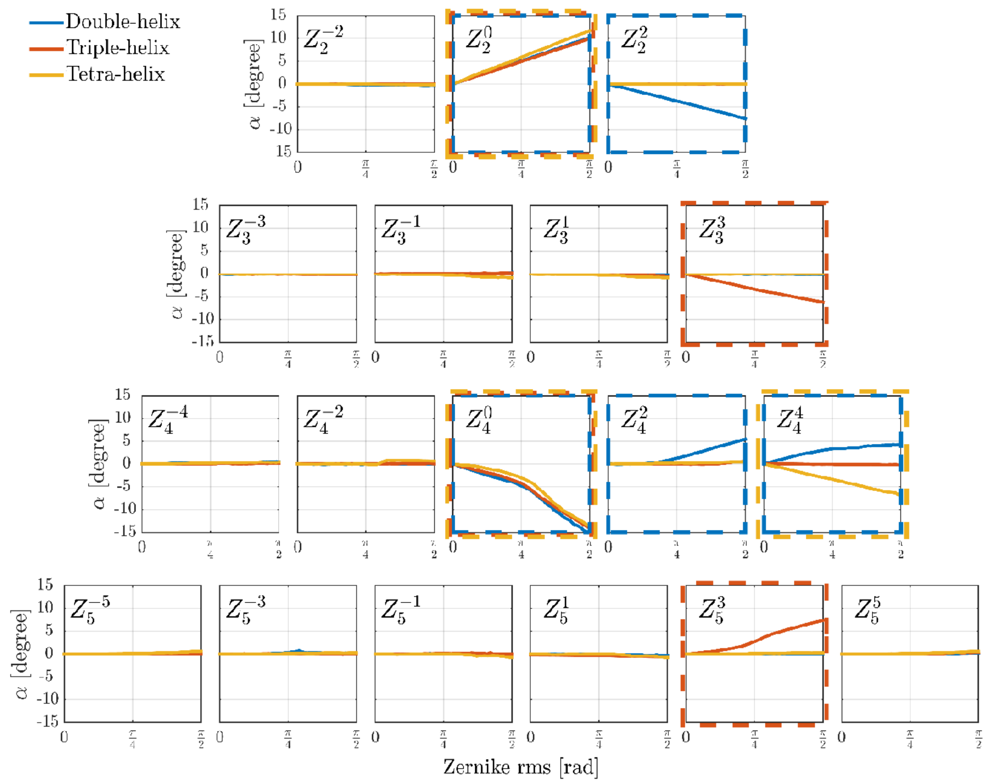


Fig. 4. Comparison of the rotation angle dependency $\alpha$ of multi-helix-PSFs on the rms phase error for the first 21 Zernike aberrations (excluding piston, tip and tilt). Aberrations that cause a significant rotation, i.e. $|\alpha(\pi/2)| > 1°$, on a particular multi-helix design are highlighted by rectangular boxes with the respective plot color.

where $D$ is the exit pupil distance to the image plane and $E$ denotes a normalization factor. In the following, only a single Zernike aberration is considered. The wave front $W(u, v)$ of the aberrated, pupil engineered system is related to the pupil phase in Eq. (5) by the wavelength $\lambda$ according to:

$$\begin{aligned} W(u,v) &= \frac{\lambda}{2\pi} \cdot \Phi(u,v) \\ &= \underbrace{\frac{\lambda}{2\pi} \cdot \Phi_p(u,v)}_{W_p} + \underbrace{\frac{\lambda}{2\pi} \cdot A_n^m \cdot Z_n^m(u,v)}_{W_n^m} \end{aligned} \tag{10}$$

and can be decomposed into a sum of the aberrated (Zernike) part $W_n^m(u, v)$ and the phase element part $W_p(u, v)$. The multi-order-helix design approach presented in section 2 demonstrates that the phase element effectively divides the wavefront $W(u, v)$ into $N$ angular segments $S_j$ in the pupil plane that are defined by the azimuthal range:

$$\frac{2\pi(j-1)}{N} \leq (\phi_u - \phi_0) < \frac{2\pi j}{N} \quad | \; j = 1, ..., N \;, \tag{11}$$

where $\phi_0$ denotes a rotational offset. Each segment $S_j$ directly corresponds to a particular PSF peak $j$. Therefore, the centroids $\langle \vec{c} \rangle_j$ of each partial wavefront $W_j(u, v)$ can be considered individually. We want to emphasize that this approximation is also applicable to the conventional design approaches based on GL-modes or Fresnel zones. The individual centroids are obtained by inserting Eq. (10) into Eq. (9), which leads to:

$$\begin{aligned}\langle\vec{c}\rangle_j &= -\frac{D}{E}\iint_{S_j}\vec{\nabla}W(u,v)\;dudv\\ &= -\frac{D}{E}\iint_{S_j}\vec{\nabla}W_p(u,v)\;dudv-\frac{D}{E}\iint_{S_j}\vec{\nabla}W_n^m(u,v)\;dudv\\ &= \langle\vec{p}\rangle_j+\langle\vec{z}_n^m\rangle_j \end{aligned}\tag{12}$$

Figure 5(a) illustrates the respective subareas $S_1$ and $S_2$ of the phase element part $W_p(u,v)$ for the double-helix design. Furthermore, the corresponding gradient vector distribution, which needs to be integrated over the subareas to determine the centroid vectors according to Eq. (9) is indicated. An equivalent plot of defocus aberration $W_2^0(u,v)$ is shown in Fig. 5(b). The respective vectors $\langle\vec{p}\rangle_j$ and $\langle\vec{z}_n^m\rangle_j$ according to Eq. (12) are indicated in Fig. 5(c) for the exemplary case of a defocus aberration on a double-helix design. Note that the centroid positions of the individual PSF peaks do not quantitatively match the peak locations detected by a Gaussian fit, which is due to the side lobes in combination with spot deformations and the background irradiance level. However, both methods to locate the PSF peaks agree on the presence or absence of rotation, which is the main goal of this theoretical investigation.

In general, the deformation of a ring of $N$ engineered PSF peaks can be described geometrically by an overall shift, a scaling, an anisotropic stretch and a rotation, provided that the deformation of the shape of the sub-spots themselves is neglected. Accordingly, we define the (scalar) measure:

$$M_n^m=\hat{z}\cdot\left(\sum_{j=1}^{N}\langle\vec{p}\rangle_j\times\langle\vec{z}_n^m\rangle_j\right)\ ,\tag{13}$$

where $\hat{z}$ is the unit vector in the $z$-direction (along optical axis). The measure $M_n^m$ is only sensitive to rotation and not affected by the other shape distortions. The detailed evaluation of the PSF

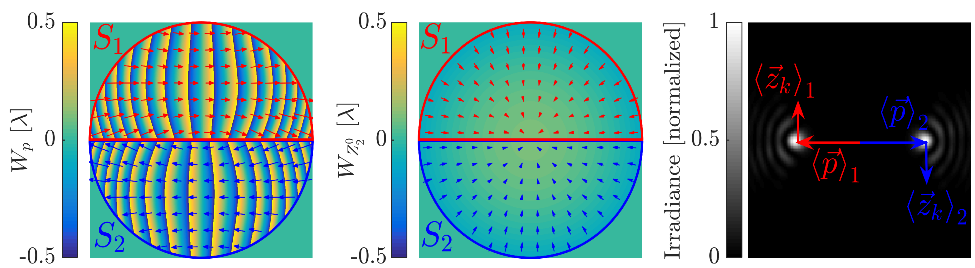


(a) (b) (c)

Fig. 5. Wavefront distribution of (a) phase element part $W_p$ and (b) defocus aberration part $W_{Z_2^0}$ (b) as well as respective gradient fields $\vec{\nabla}W_p$ and $\vec{\nabla}W_{z4}$. The two highlighted subareas $S_1$ and $S_2$ directly correspond to the two peaks of the double-helix PSF. (c) PSF distribution associated with $W_p$. The direction of the centroid vectors $\langle\vec{p}\rangle$ and $\langle\vec{z}_k\rangle$ are indicated for both subareas $S_1$ and $S_2$, respectively.

rotation measure $M_n^m$ is disclosed in the appendix (see section 6). The theoretical analysis proves that an aberrated wavefront $W_n^m$ only leads to rotation of a multi-order-helix PSF (i.e. $M_n^m \neq 0$), if the azimuthal order $m$ is an integer multiple $\kappa$ of the peak number $N$ according to the derived condition

$$m=\kappa\cdot N\quad\mid\ \kappa=0,1,2,\ldots\tag{14}$$

which provides the major outcome of the assessment. It particularly demonstrates that all types of multi-order-helix PSFs are sensitive to spherical aberration of all orders ($Z_4^0$,$Z_6^0$, ...). Moreover, it reveals that double-helix designs are sensitive to astigmatism of all orders ($Z_2^{\pm 2}$,$Z_4^{\pm 2}$, ...), whereas higher-order designs are not. In fact, triple-helix designs are sensitive to trefoil of all orders ($Z_3^{\pm 3}$,$Z_5^{\pm 3}$, ...), tetra-helix designs to tetrafoil etc. In addition, the rotation measure for odd Zernike aberrations in Eq. (34) vanishes for the particular case of $\phi_0 = 0$. These results are in agreement with the numerical simulations performed in section 3.1 and qualitatively match the rotation angle investigation shown in Fig. 4. In general, the analysis verifies that a higher number of peaks $N$ leads to less Zernike modes that result in (unwanted) rotation and thus provides an increased aberration robustness with regard to monocular depth measurements. However, it should be recalled from section 2 that a larger parameter $N$ results in a reduced depth range of $[-\pi/N, \pi/N]$ at the same time.

## 4. Experimental results

### *4.1. Optical setup*

A demonstration setup based on a hybrid optical imaging system is realized according to the system concept proposed in [15]. The three phase element designs studied in section 3 (double-, triple- and tetra-helix) are implemented using state-of-the-art micro-optics manufacturing processes on wafer-scale. A thin photoresist layer is initially spun on a borosilicate glass substrate and subsequently structured using the LED writing lithography approach presented by Eckstein et al. in [27]. The next steps provide a significant advancement in the manufacturing of phase elements for monocular depth estimation compared to previous elements [9, 15]. The surface profile of the photoresist layer is directly transferred onto the borosilicate glass substrate by applying reactive-ion-etching to generate a highly accurate and robust imprinting tool. Subsequently, a thin polymer layer is deposited on a second borosilicate glass substrate. The final wafer is obtained by transferring the surface profile of the tool to the polymer layer of the second substrate using UV-imprinting. We want to emphasize that the etched borosilicate glass tool potentially allows for manufacturing large numbers of polymer-on-glass wafers containing the respective phase elements. In addition to the high cost-efficiency, the utilized hybrid polymers, such as ORMOCERE [28], provide increased temperature and mechanical stability, as well as improved transparency over the entire visual range compared to previous elements that were directly realized in a photo resist layer. However, the main challenge relies in minimizing surfaces distortions during the replication process, which would directly compromise the performance of the CGH with respect to the introduced wave front error. The final optical elements are obtained by dicing the manufactured wafers and mounting the individual designs in customized, opaque frames, which define circular apertures of 10 mm diameter. The measured surface profiles $h(x, y)$ of the tool and the replication are plotted in Fig. 6 for the double-helix CGH design. The plot shows that the profile of the tool element accurately complies with the phase element design shown in Fig. 1 (g). Moreover, the surface measurement of the replicated element demonstrates the successful transfer of the tool profile using UV replication. The apparent shape deviation is likely due to a bending of the 1 $mm$ thin replication substrate, which does, however, not affect the PSF distribution significantly. A quantitative analysis of the residual wavefront error would additionally require the profile of the substrates back side, which is not directly accessible using a white light interferometer measurement.

An optical system based on two achromatic doublets (Thorlabs AC254-200-A and AC254-100-A) is set up to verify the functionality of the new phase elements and further to demonstrate the enhanced aberration robustness of high-order-helix designs. A frame with a particular CGH design can be placed in front of the two lenses, where it defines the entrance pupil of the optical demonstration system. The resulting setup, which is characterized by a focal length of 71 $mm$ and an F-number of 7.4, is placed in front of a commercial camera system (AVT Pike F-505). The monochrome 2/3 inch CCD sensor (Sony ICX625) provides a pixel size of 3.45 $\mu m$ and a total pixel count of $2452 \times 2054$, which leads to an overall field of view (FOV) of 114 $mm \times 96$ $mm$ at the nominal object distance of 1 $m$. The system provides diffraction limited performance on the optical axis for the design wavelength of 540 $nm$. However, it is intentionally subject to significant off-axis aberrations dominated by astigmatism and field curvature.

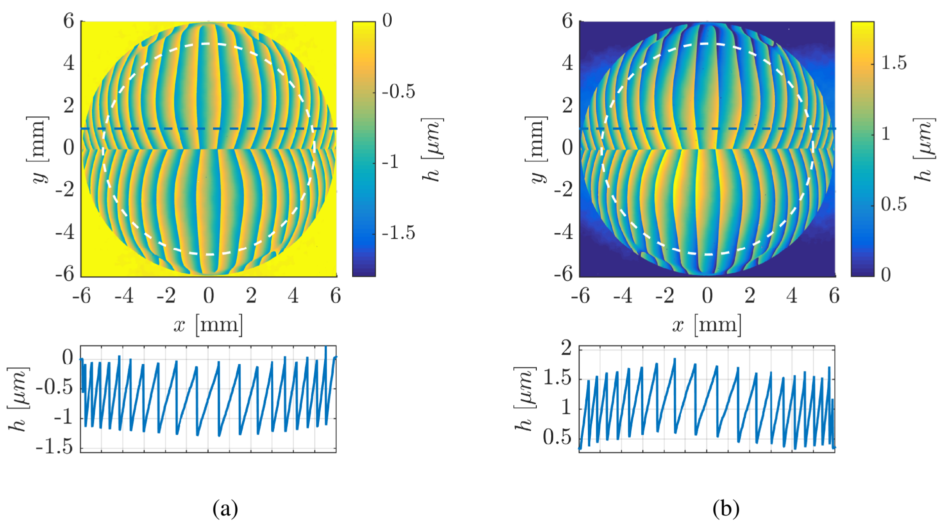


Fig. 6. Top: Measured surface profile height $h(x, y)$ of (a) the tool and (b) the replication of the double-helix CGH design. The dashed white circle indicates the aperture size of 10 mm used in the optical setup. Bottom: horizontal cross-section of the profile height $h(x)$ at $y = 1$ $mm$ as indicated by dashed blue lines in the respective upper plots.

### 4.2. Demonstration of on-axis PSF rotation

Initially, the depth dependent rotation of the engineered PSF is investigated for the three CGH designs of interest. To this end, an on-axis LED point source with a peak irradiance at 540 $nm$ is imaged for different object distances in a range between 860 $mm$ and 1180 $mm$, which covers the optimized 90° rotation range of the tetra-helix PSF design. It is pointed out that the double- and triple helix PSFs continue rotating beyond this range. The top part of Fig. 7 illustrates the respective PSF distributions at multiple object distances. The displayed irradiance levels are normalized to the maximum peak value at $z = 1000$ $mm$ for each design, respectively. The individual plots demonstrate a continuous PSF rotation, featuring clearly defined peaks. Solely one of the tetra helix PSF spots exhibits accelerated spreading with increasing object distance. This may be attributed to minor CGH distortions introduced during the manufacturing process, which affect the individual focus position as well as the depth of focus of the PSF spots. Nevertheless, Fig. 7 demonstrates that the helical PSF shape of all realized PSFs is maintained throughout an extended axial range of at least 300 $mm$. Accordingly, the axial range significantly extends over the diffraction limited depth of field of the nominal PSF, which is in the order of $\lambda/\mathrm{NA}^2 \approx 22$ $mm$. The bottom part of Fig. 7 shows a close to linear dependency of the rotation angle $\alpha$ on the object distance $z$. The individual data points are obtained by fitting $N$ Gaussian peaks to the respective PSF images and averaging over the fitted angular changes $\Delta\alpha_i$ according to Eq. (8). The center of each helical PSF is determined by calculating the center of gravity of the individual distributions. Note that the respective localization accuracy, which is limited by noise and a finite sampling, is in

Research Article Vol. 26, No. 4 | 19 Feb 2018 | OPTICS EXPRESS 4886


the same order as the accuracy of the peak localization and adds a comparable error contribution to the overall rotation angle measurement. In fact, the angle determination for the tetra-helix design is ambiguous for angles $|\alpha| > 45°$, which generally prohibits a depth retrieval beyond this angle. Prior knowledge on the rotation is used in Fig. 7 to circumvent these ambiguities for comparison purposes only. The PSFs feature comparable rotation rates $\Delta\alpha/\Delta z$ on the order of $0.3\ °/mm$, which is in accordance with the design parameters of the three CGHs due to the similar values of $N \cdot L$. Moreover, the peak distances $p$ of approximately 12 pixels also agree for the three designs. Finally, we point out that the proper functionality of the replicated phase elements with respect to the PSF rotation confirms the successful manufacturing by UV replication. Thus, we verified a cost-efficient manufacturing approach of pupil engineering CGHs with enhanced optical, thermal and mechanical properties compared to previous photoresist-on-glass elements for monocular, three-dimensional imaging.

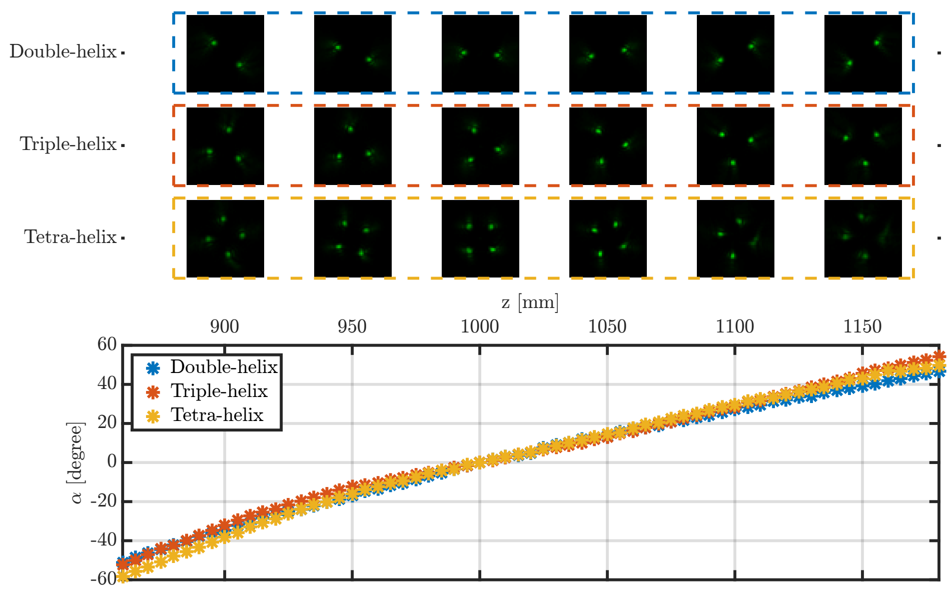


Fig. 7. Top: Measured on-axis distributions of the engineered double-, triple- and tetra-helix PSFs at multiple object distances $z$ ($\lambda = 540\ nm$). Bottom: Corresponding dependency of the rotation angle $\alpha$ on the object distance $z$.

### *4.3. PSF rotation across an extended field of view*

#### 4.3.1. Image acquisition

We exploit the severe off-axis aberrations of the demonstration setup in order to provide experimental verification of the superior aberration robustness of high-order-helix designs. To this end, the pupil engineered image of a planar screen located at the nominal object distance of $1\ m$ and homogeneously illuminated by the previously applied LED source, is acquired. Figure 8(a) shows the nominal image distribution if no phase element is mounted inside the aperture stop. The white screen features a random pattern of black dots, which provide the required spatial features for the following analysis. It can already be observed that the image quality is significantly decreased at the edges of the field of view due to field curvature and astigmatism. The three CGHs with the designs under investigation are successively incorporated to image the same scene. For comparison purposes, only the central portion of the overall FOV is shown in Fig. 8(b)-8(e) for each of the three PSF designs in addition to the nominal case without a

CGH, respectively. The shown subimages illustrate the effect of pupil engineering, which can be modeled as a convolution of the helical PSFs, shown in Fig. 7, with the nominal subimage shown in Fig. 8(b).

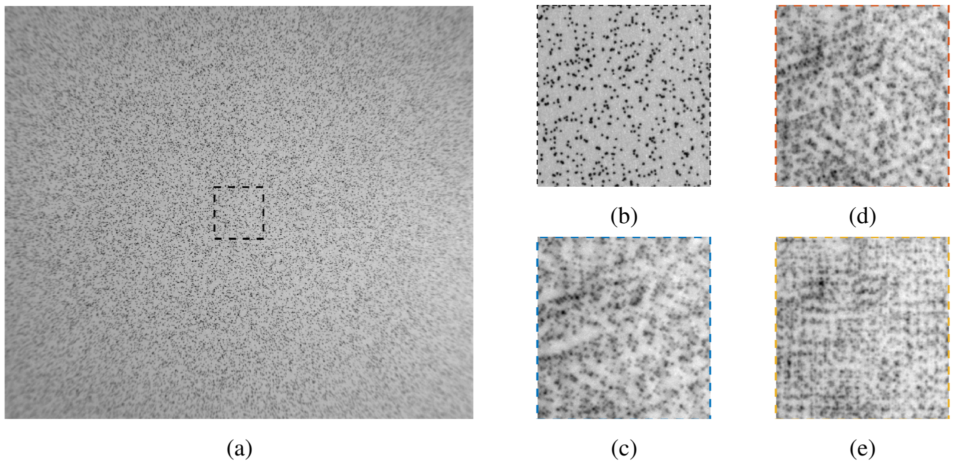

Fig. 8. (a) Nominal distribution of the imaged test screen if no CGH is implemented in the demonstration system. The subimage shown in (b) correspond to the inset indicated in (a). The subimages (c)-(e) show the same part of the image after the double-, triple- and tetra-helix CGHs are implemented in the demonstration system, respectively.

#### 4.3.2. Cepstrum distribution

The cepstrum approach previously introduced by us [15] is used in order to extract the lateral rotation angle distribution $\alpha(x, y)$ of the engineered PSFs from the acquired images. This method is based on calculating the image cepstrum in a local environment around $(x, y)$ and searching for peaks in the cepstrum domain. The location of the cepstrum peaks provides the information on the local PSF rotation. The approach was initially developed for double-helix designs but can be extended in order to accommodate for higher-order-helix PSFs. In fact, the number of first order peaks $K$ in the cepstrum domain is equal to $N(N-1)$ for the rotating PSF designs introduced in section 2. However, peaks in the cepstrum may overlap due to symmetry in the respective PSF. This is the case for high-order-helix PSFs with even peak numbers and $N > 2$. The corresponding number of distinguishable peaks reduces to $N^2/2$. In addition, aberrations can change the number of cepstrum peaks that can be distinguished by changing the PSF shape and thus eliminating or adding symmetry in the PSF peak locations.

Figure 9 illustrates the cepstrum of the $256 \times 256$ pixel subimages shown in Fig. 8(c)-8(e), respectively, after a Hann window is applied to mitigate edge effects. Note that these distributions are smoothed and the regions of interest are truncated as described in [15] in order to isolate first order cepstrum peaks. It can be observed that the double- and triple-helix designs exhibit clearly distinguishable cepstrum peaks with a constant radial distance and comparable magnitudes. The peaks of the tetra-helix design are, however, located at different radial distances and partially overlap, which results in 8 distinguishable peaks.

#### 4.3.3. Rotation angle analysis

The information on the location of the cepstrum peaks is used to determine to the rotation angle $\alpha$ and in that way enable a local depth estimation. Due to the complex tetra-helix cepstrum distribution with varying peak distances and overlapping peaks, we limit ourselves to the double-

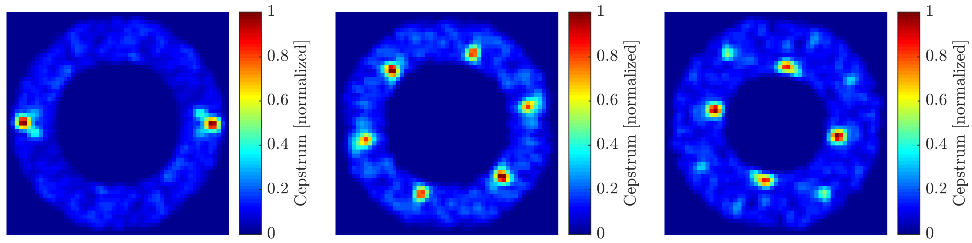


(a) Double-helix (b) Triple-helix (c) Tetra-helix

Fig. 9. Processed Ccepstrum distributions of the subimages shown in Fig. 8(c)-8(e).

and triple-helix design in order to demonstrate the difference in aberration robustness. The local cepstrum distributions are calculated for each image position $(x, y)$ in a $256 \times 256$ pixel environment. The first order cepstrum peaks are located by fitting Gaussian functions to the peaks. The overall rotation angle $\alpha$ directly corresponds to the average of the $K/2$ peak angle changes in the cepstrum domain. It is noted that the cepstrum approach reduces the unambiguous angular rotation range of the triple-helix designs by a factor of two, i.e. $[-30°, 30°]$, due to the PSF symmetry. The calculated overall rotation angle distribution of the test images are shown in Fig. 10(a) and 10(c). It can be observed that $\alpha(x, y)$ is increasing towards the edges of the FOV despite the constant depth of the imaged screen. This observation can be related to a significant field curvature, a field dependent defocus aberration ($Z_2^0$) that results in undesired rotation for all multi-order-helix designs. Note that a comparison between the two plots yet reveals a significant shape deviation.

In order to eliminate the effect of field curvature and enable the analysis of effects from other aberrations, a parabolic function is fitted and subtracted from the rotation angle distribution $\alpha(x, y)$. In practice, this could be achieved by incorporating a customized field flattening element in close proximity to the image sensor. Figure 10(c) and 10(d) show the respective angular distributions $\alpha_r(x, y)$ with field curvature removed. The remaining error is mainly due to field dependent astigmatism, which results in false PSF rotation for the double-helix design, as predicted in section 3. In contrast, the triple-helix design does not suffer from this error, which allows for a significantly increased accuracy of the depth measurement. The RMS error in the angle estimation over the entire FOV is reduced from $1.7°$ to $0.3°$, which demonstrates the superior aberration robustness of a high-order-helix PSF compared to the conventional double-helix PSF shape. We emphasize that the improved robustness is particularly crucial for low-NA, large FOV optical systems in machine vision or automotive applications, where astigmatism is one of the major aberrations.

## 5. Conclusion

A novel approach for the design of phase elements to generate engineered, multi-order-helix PSFs with a depth dependent rotation is presented. The approach is based on a combination of two previously introduced design methods and enables PSF distributions with a large peak separation and a high peak confinement over an extended depth range. In addition, it allows for the design of purely refractive optical elements, which potentially provide an enhanced imaging performance with respect to color artifacts. The performance of the novel designs is assessed based on Cramér-Rao Lower Bound analysis. The influence of Zernike aberrations on the rotation of engineered, multi-order-helix PSFs has been investigated. The numerical analysis revealed that high-order-helix designs ($N > 2$) facilitate a more robust depth estimation in the presence of aberrations. In particular, a theoretical assessment showed that only Zernike aberrations with an

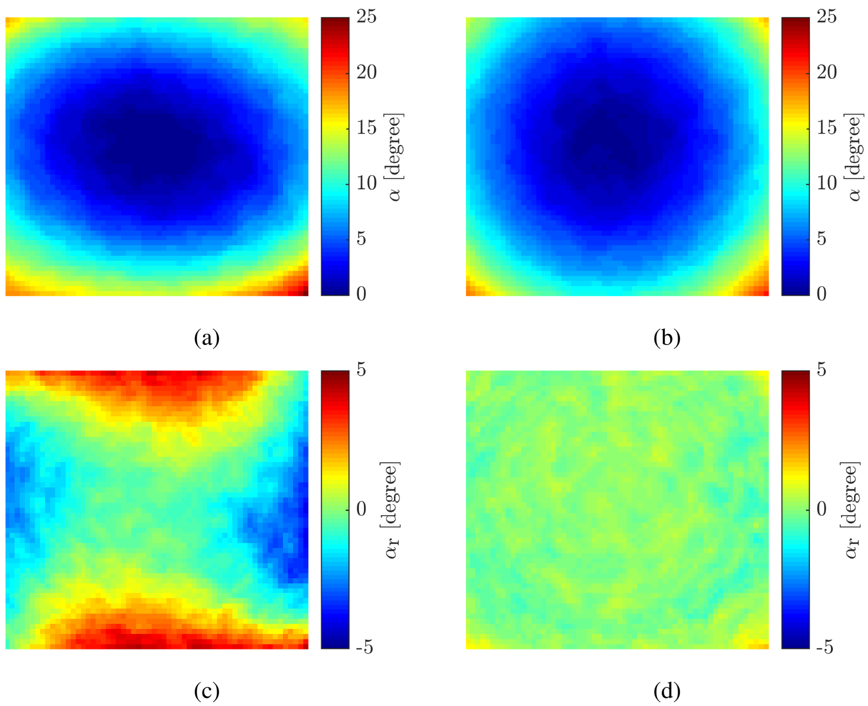


Fig. 10. Measured rotation angle distribution $\alpha$ of the imaged demonstration scene using a (a) double- and (b) triple-helix PSF. (c) and (d) show the residual rotation angle distributions $\alpha_{\mathrm{r}}(x, y)$ for the two cases after eliminating the effect of field curvature by fitting and subtracting a parabolic function from $\alpha(x, y)$.

azimuthal order $m = \kappa \cdot N$ ($\kappa = 0, 1, 2, \ldots$) lead to PSF rotation.

Furthermore, the successful manufacturing of cost-efficient phase elements based on UV-replication on wafer-scale is verified. A demonstration system has been implemented to demonstrate the proper depth dependent rotation of novel triple- and tetra-helix PSF designs. In addition to a theoretical assessment, the superior aberration robustness of high-order-helix designs is demonstrated experimentally by analyzing the rotation angle distribution of an imaged scene.

The main goal of this paper is to provide a basis for balancing optical aberrations during the design process of pupil engineered, 3D imaging systems, which require minimized unwanted PSF rotation for an accurate monocular depth measurement. In contrast, future work will include investigating the possibility for a dedicated measurement of aberrated wavefronts using optical systems that feature a multi-order-helix PSF. In particular, we aim to exploit the effect of different aberrations on the shape of the PSF in order to extract information on present aberrations for potential applications such as adaptive optics.

It is mentioned that higher order helix PSFs can also find application in the field of single molecule imaging, where imaging at relatively large depth in cells and tissue gains considerable importance, implying that aberration robust PSFs could potentially be of use.

## 6. Appendix: evaluation of rotation measure $M_n^m$

The evaluation of the measure for PSF rotation $M_n^m$, as introduced in Eq. (13), is provided in the following. The centroid positions $\langle \vec{p} \rangle_j$ of each multi-order-helix PSF peak $j = 1, 2, \ldots, N$ can be

Optics EXPRESS

written as:

$$\langle \vec{p} \rangle_j = p \cdot \begin{pmatrix} \cos\phi_j \\ \sin\phi_j \end{pmatrix} \quad , \tag{15}$$

where:

$$\phi_j = \phi_0 + \frac{\pi}{2} - \frac{\pi}{N} + j\frac{2\pi}{N} \tag{16}$$

according to the design approach described in section 2. After transition to polar coordinates, the position vectors can be expressed as:

$$\langle \vec{p} \rangle_j = p\cos(\phi - \phi_j)\hat{\rho} - p\sin(\phi - \phi_j)\hat{\phi} \quad , \tag{17}$$

where $\hat{\rho}$ and $\hat{\phi}$ are unit vectors in the radial and azimuthal direction, and $p$ is the distance of the peak to the PSF center. The Zernike centroid vector $\langle \vec{z}_n^m \rangle_j$ is determined by the gradient in polar coordinates according to:

$$\langle \vec{z}_n^m \rangle_j = \left\langle -\vec{\nabla} W_n^m \right\rangle_j = \left\langle -\frac{\partial W_n^m}{\partial \rho}\hat{\rho} - \frac{1}{\rho}\frac{\partial W_n^m}{\partial \phi}\hat{\phi} \right\rangle_j \tag{18}$$

Inserting Eq. (17) and Eq. (18) into the rotation measure defined in Eq. (13) leads to the following expression:

$$M_n^m = p \cdot \sum_{j=1}^{N} \left\langle -\frac{1}{\rho}\cos(\phi - \phi_j)\frac{\partial W_n^m}{\partial \phi} - \sin(\phi - \phi_j)\frac{\partial W_n^m}{\partial \rho} \right\rangle_j \tag{19}$$

The integration variable $\psi = 2\pi j/N + \phi_0 - \phi$ is used for the average over the pupil in Eq. (19) so that for all segments $j$ the integration range is:

$$0 \leq \psi \leq \frac{2\pi}{N} \tag{20}$$

The rotation measure then follows as:

$$\begin{aligned} M_n^m = \frac{pD}{E} \int_{\rho=0}^{1} \int_{\psi=0}^{2\pi/N} \sum_{j=1}^{N} \Bigg[ & \frac{1}{\rho}\sin\left(\frac{\pi}{N} - \psi\right) \frac{\partial W_n^m\left(\rho, \frac{2\pi j}{N} + \phi_0 - \psi\right)}{\partial \psi} \\ & + \cos\left(\frac{\pi}{N} - \psi\right) \frac{\partial W_n^m\left(\rho, \frac{2\pi j}{N} + \phi_0 - \psi\right)}{\partial \rho} \Bigg] \rho d\rho d\psi \end{aligned} \tag{21}$$

First, the rotation measure is considered for even Zernike aberration functions $Z_n^m$ defined in Eq. (6), which includes modes with $m = 0$. It can be written as:

$$M_n^m = \frac{2\pi p D A_n^m}{\lambda E} \left[ m F_{ss} \int_{\rho=0}^{1} R_n^m(\rho) d\rho + F_{cc} \int_{\rho=0}^{1} \rho \frac{\partial R_n^m(\rho)}{\partial \rho} d\rho \right] \tag{22}$$

using the definition of $W_n^m$ in Eq. (10). The two respective integrals over the azimuthal angle $\psi$ are defined by:

$$F_{ss} = \int_{\psi=0}^{2\pi/N} \left[ \sin\left(\frac{\pi}{N} - \psi\right) \sum_{j=1}^{N} \sin\left(\frac{2\pi j m}{N} + m\phi_0 - m\psi\right) \right] d\psi \tag{23}$$

$$F_{cc} = \int_{\psi=0}^{2\pi/N} \left[ \cos\left(\frac{\pi}{N} - \psi\right) \sum_{j=1}^{N} \cos\left(\frac{2\pi j m}{N} + m\phi_0 - m\psi\right) \right] d\psi \tag{24}$$

Optics EXPRESS

In fact, both integrals equal zero unless $m$ is a multiple of the PSF peak number $N$ according to:

$$m = \kappa \cdot N \quad | \ \kappa = 0, 1, 2, \ldots \tag{25}$$

For these specific cases, the integrals take the form:

$$F_{ss} = \frac{N}{\kappa^2 N^2 - 1} \left[ -2\kappa N \sin\left(\frac{\pi}{N}\right) \cos\left(\kappa N \phi_0\right) \right] \tag{26}$$

$$F_{cc} = \frac{N}{\kappa^2 N^2 - 1} \left[ -2 \sin\left(\frac{\pi}{N}\right) \cos\left(\kappa N \phi_0\right) \right] \tag{27}$$

The latter integral over the radial coordinate in Eq. (22) can be simplified by partial integration according to:

$$\int_{\rho=0}^{1} \rho \frac{\partial R_n^m(\rho)}{\partial \rho} d\rho = 1 - \int_{\rho=0}^{1} R_n^m(\rho) d\rho \tag{28}$$

The remaining integral over the the radial Zernike polynomial $R_n^m$ turns out to be:

$$\int_{\rho=0}^{1} R_n^m(\rho) d\rho = \frac{(-1)^{(n-m)/2}}{(n+1)} \tag{29}$$

This result was found using Mathematica, but no formal proof could be found in the literature. Thus, the rotation measure in Eq. (22) takes the form:

$$M_n^m = \frac{2\pi p D A_n^m}{\lambda E} \left[ F_{cc} + (m F_{ss} - F_{cc}) \left( (-1)^{(n-m)/2} \cdot \frac{1}{(n+1)} \right) \right] \tag{30}$$

Inserting Eq. (26) and Eq. (27) in Eq. (30) and considering only Zernike aberrations that fulfill condition (25) results in:

$$M_n^{\kappa N} = \frac{-4\pi p D A_n^{\kappa N} N}{\lambda E(\kappa^2 N^2 - 1)} \sin\left(\frac{\pi}{N}\right) \cos\left(\kappa N \phi_0\right) \left[ 1 + \left( (-1)^{(n-\kappa N)/2} \cdot \frac{(\kappa^2 N^2 - 1)}{(n+1)} \right) \right] \tag{31}$$

For odd Zernike aberration functions defined in Eq. (7) the two integrals over the azimuthal angle $\psi$ in Eq. (21) also equal zero unless condition (25) is fulfilled. In this case, the respective integrals take the form

$$F_{sc} = \frac{N}{\kappa^2 N^2 - 1} \left[ 2\kappa N (-1)^{\kappa} \sin\left(\frac{\pi}{N}\right) \sin\left(\kappa N \phi_0\right) \right] \tag{32}$$

$$F_{cs} = \frac{N}{\kappa^2 N^2 - 1} \left[ -2(-1)^{\kappa} \sin\left(\frac{\pi}{N}\right) \sin\left(\kappa N \phi_0\right) \right] \tag{33}$$

and the rotation measure results in

$$M_n^{-\kappa N} = (-1)^{\kappa} \frac{-4\pi p D A_n^{\kappa N} N}{\lambda E(\kappa^2 N^2 - 1)} \sin\left(\frac{\pi}{N}\right) \sin\left(\kappa N \phi_0\right) \left[ 1 - \left( (-1)^{(n-\kappa N)/2} \cdot \frac{(\kappa^2 N^2 + 1)}{(n+1)} \right) \right] \tag{34}$$

## Funding

German Federal Ministry of Education and Research (BMBF) (13N13667).

## Acknowledgments

The authors would like to thank Marko Stumpf, Andre Matthes and Peter Dannberg for manufacturing the CGHs, as well as Jens Dunkel for performing the surface profile measurements.